1 **ORIGINAL PAPER**

2 # The historical case of Paricutin volcano (Michoacán, México):
3 # challenges of simulating lava flows on a gentle slope
4 # during a long-lasting eruption

5 **Laura Becerril[1,2]** · **Patricia Larrea[3,4]** · **Sergio Salinas[5]** · **Sophie Mossoux[6]** ·
6 **Dolors Ferrés[7]** · **Elisabeth Widom[4]** · **Claus Siebe[8]** · **Joan Martí[2]**

9 **Abstract**
10 Simulating lava flows on a gentle slope is complex since they can propagate in a wide range
11 of directions. It is an even greater challenge to define lava flow trajectories when an erup-
12 tion lasts over several years and flows cool down, changing the surrounding topography. In
13 this study, we test Q-LavHA, an open source plug-in that simulates lava flow inundation
14 calculating its probability, and using Paricutin's eruption (1943–1952) in central Mexico as
15 a case study. We have appropriately calibrated the Q-LavHA plug-in for the Paricutin case
16 study, which provides insights on how to better model lava flows in gentle terrain. From
17 this work, we observe that each phase is characterized by a unique set of parameters requir-
18 ing a careful calibration and that low-relief topographies require special consideration. Our
19 findings could be useful for real-time hazard evaluation in future volcanic scenarios in the
20 Michoacán–Guanajuato volcanic field and elsewhere, where new monogenetic eruptions
21 similar to Paricutin can be expected.

22 **Keywords** Parícutin volcano · Michoacán–Guanajuato volcanic field · Monogenetic
23 volcanism · Lava flow simulations · Volcanic hazard assessment · Q-LavHA

24 ## 1 Introduction

25 In recent decades, many studies have been motivated by the necessity to understand
26 the hazards associated with volcanic eruptions, which is especially important where
27 volcanic fields are located near population centers (e.g., Loughlin et al. 2015; Rymer
28 2015, etc.). Improving lava flow hazard assessment is a significant and challenging task
29 of modern volcanology (Cordonnier et al. 2016). Current volcanological studies pursue
30 important objectives such as: to reproduce accurately the pathway behavior of lavas,
31 to develop models that include digital elevation models (DEMs) and allow real-time
32 eruption updates, to perform optimal simulations in gently sloping terrain, etc. Lava
33 flows with negative economic impact average 60 events per century (Booth 1979). They

A1 ✉ Laura Becerril
A2 laura.becerril@sernageomin.cl

A3 Extended author information available on the last page of the article

| Journal : **SmallCondensed 11069** | Article No : **4607** | Pages : **21** | MS Code : **4607** | Dispatch : **9-2-2021** |

Natural Hazards

34 generally flow slowly and their trajectories are mainly governed by topography; there-
35 fore, the identification of areas at risk from new eruptions is fundamental for mitigating
36 potential human fatalities and material damage.

37   Hazard evaluation and contingency planning in volcanic areas depend heavily on
38 hazard maps and simulation models, which themselves rely on good geological–volcan-
39 ological knowledge of the volcanic area or volcano (Martí 2017). Much effort has been **AQ2**
40 invested toward forecasting the timing, nature, and impact of future eruptions of polyge-
41 netic volcanoes, where eruptions can occur from the summit or on the flanks, affecting
42 areas distant from each other (e.g., Mt Etna; Crisci et al. 2010; Del Negro et al. 2013).
43 However, monogenetic volcanoes, which erupt only once (Walker 2000), can form in
44 vast areas with a very low eruptive frequency (on the order of 10^{-4}–10^{-5} eruptions/year;
45 Valentine and Connor 2015), and with a relatively small eruptive volume (< 1 km^3 of
46 mafic magma; Kereszturi and Németh 2012). These facts commonly lead to the percep-
47 tion that these volcanoes pose less potential danger than polygenetic ones. Neverthe-
48 less, they present special problems, as they tend to arise unexpectedly in time and space
49 within distributed volcanic fields. Forecasting the location, timing, types and impact/
50 effects of the related hazards in distributed volcanic areas represents an ongoing chal-
51 lenge that has been addressed over the last 50 years through probabilistic and geological
52 approaches (e.g., Bartolini 2014; Bertin et al. 2019 and references therein).

53   Mexico hosts the largest subduction-related distributed volcanic field on Earth, the
54 Michoacán–Guanajuato Volcanic Field (MGVF; Hasenaka and Carmichael 1985) in the
55 Trans-Mexican Volcanic Belt (TMVB; Fig. 1). The MGVF has experienced two impor-
56 tant historic eruptions, Jorullo (1759–1774) and Paricutin (1943–1952), which caused
57 serious social, environmental, and economic disruptions (Luhr and Simkin 1993; Inbar
58 et al. 1994; Guilbaud et al. 2011). This monogenetic field poses risk to rural and urban
59 centers in Michoacán and Guanajuato, mainly due to lava flows but also to the likely
60 ashfall that can reach other populated areas, including Mexico City (Siebe and Macias
61 2006). However, the hazard of future monogenetic activity in the MGVF has not yet
62 been well assessed, even though several research efforts have been made in the area
63 (e.g., Connor 1987; Delgado-Granados and Jenkins 2015). Studies dealing with erup-
64 tion recurrence rates, spatial and temporal distribution of the volcanoes, composition
65 and eruptive style, and the tectonic control of this type of volcanism in the whole dis-
66 tributed field are not yet sufficient to facilitate hazard assessments and development of
67 monitoring strategies.

68   This paper focuses on the Paricutin eruption, which started on a gently sloping pre-
69 eruption topography, with prevailing slopes ranging from 0° to 9° with no preferred
70 downslope direction (Supplementary Material 1). The existence of detailed lava flow
71 distribution maps (Luhr and Simkin 1993) and reconstructed paleotopography maps
72 (Larrea et al. 2017) for all of the eruptive phases makes this volcano an ideal candi-
73 date to test lava flow simulation tools. This research (a) presents a comparison of the
74 erupted and simulated Paricutin lava flows using Q-LavHA (Mossoux et al. 2016) and
75 (b) explores the strengths and limitations of lava flow invasion probability simulation
76 tools such as Q-LavHA, to better understand the main parameters controlling past lava
77 flow emplacement and with special emphasis on the use of this application in low-relief
78 areas. In addition, this study, together with the previous geochemical, morphometric,
79 and volumetric characterization of Paricutin (Larrea et al. 2017, 2019a, b, 2021), pro-
80 vides the first comprehensive integration of data from a historical eruption with vol-
81 canic simulations for evaluating volcanic hazard in the MGVF.
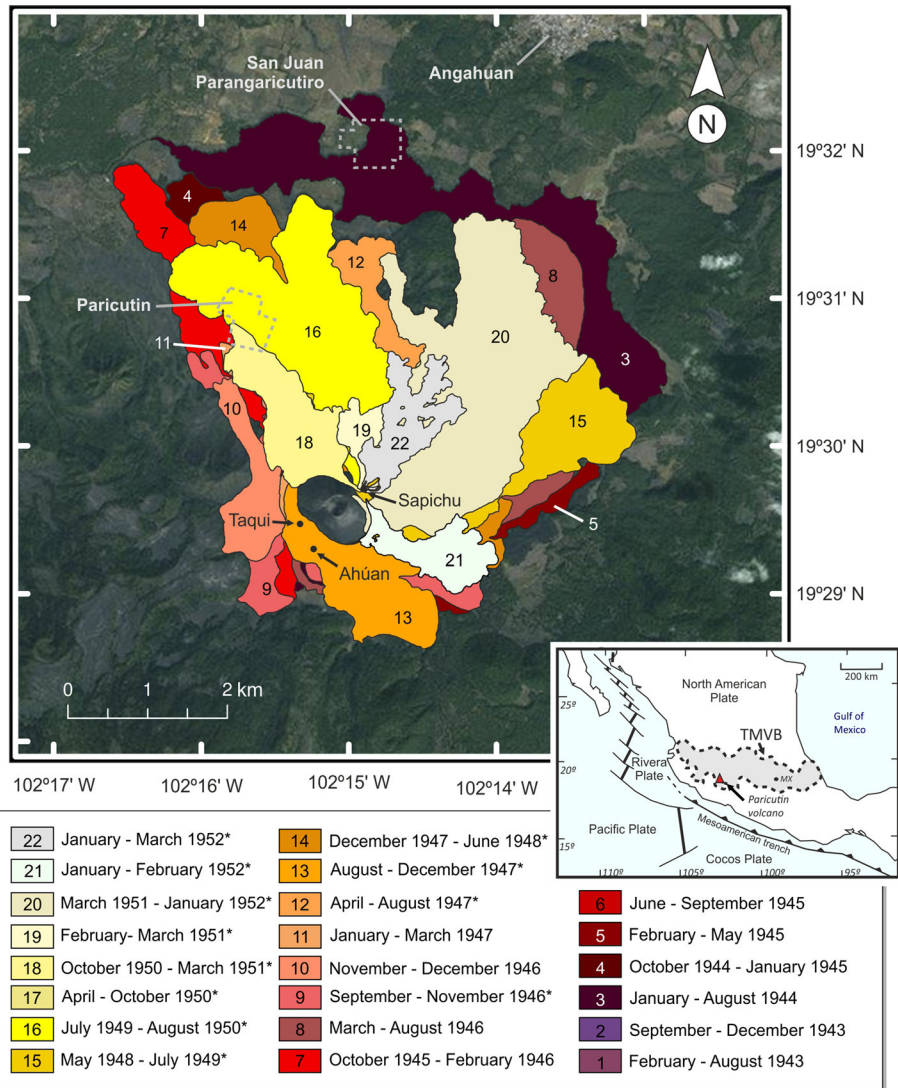
Fig. 1 Geological map of Paricutin volcano with the 22 lava eruptive phases considered in this work and modified after Luhr and Simkin (1993) and Larrea et al. (2017). Locations of the most active vents during the eruption (main cone-Paricutin, Sapichu, Taqui, and Ahúan) are also shown. The modified eruptive phases are denoted in the legend with an asterisk; see Methodology section for details. Lava eruptive phases 1, 2, 6, and 17 are not exposed on the surface because they have been covered by most recent lava flows. Inset map shows the geotectonic map of Mexico with the location of the Trans-Mexican Volcanic Belt (TMVB), Mexico City (MX), and Paricutin volcano

2 The 1943–1952 Paricutin eruption and its lava flow field

Paricutin volcano is located ~ 320 km west of Mexico City and belongs to the MGVF (Fig. 1), which contains more than 1100 Quaternary eruptive centers within an area of ~ 40,000 km^2 (Hasenaka 1994). Its eruption initiated near the village of San Juan Parangaricutiro on the

| Journal : **SmallCondensed 11069** | Article No : **4607** | Pages : **21** | MS Code : **4607** | Dispatch : **9-2-2021** |

Natural Hazards

February 20, 1943, and ended 9 years later on the March 4, 1952 (Luhr and Simkin 1993), forming a lava field with a total covered area of ~25 km² and a volume of ~1.6 km³ (DRE; Larrea et al. 2017) It built a main cone of ~240 m in height above surrounding ground (~2800 m asl) (the total cone elevation considering its current height in addition to the area buried at its foot by lava flows is 430 m) that significantly modified the original topography of the area (Supplementary Material 1). This eruption directly impacted more than 2500 people, burying the towns of San Juan Parangaricutiro and Paricutin, and damaging the villages of Zirosto, Zacán, and Angahuan (Nolan and Gutiérrez 1979) (Fig. 1). In addition, there were many social and economic impacts due to the loss of assets, farmland, and the relocation of the inhabitants to other communities. Currently, more than 75 years after the termination of the eruption, the volcano is a tourist attraction that represents an important source of income for the surrounding villages.

The eruption started, after 45 days of precursory seismicity, with continuous low-magnitude explosive activity that ejected pyroclastic material toward the southwest from the first vent, which opened as a fissure crossing a gently sloping area (main slopes from 0° to 9°; Supplementary Material 1) (Foshag and González-Reyna 1956; McBirney et al. 1987; Yokoyama and De la Cruz-Reyna 1990). This gentle pre-eruptive topography presented minor slopes that mostly ranged from 0° to 9° with no preferential downslope direction (Figure S1 in Supplementary Material 1), although small gullies related to the pre-eruption drainage network modeled the landscape with slopes up to 83° (Table S1 in Supplementary Material 1). On the second day, from the newly formed 50-m-high horseshoe-shaped cinder cone, the first lava erupted (Quitzocho flow; Ordoñez 1943). In the following months and years, the eruption was characterized by variations in its effusion rate (between 2 and 14 m³/s) which decreased progressively after 1950 (Larrea et al. 2017). In addition, an overall increase in the effective viscosity of the magma (0.9–2.38·10³ Pa·s), a shift in the active vents (main cone-Paricutin and secondary vents-Sapichu, Taqui, and Ahuán, Fig. 1), and a variation in the importance of effusive relative to explosive activity throughout the 9 years of eruption were observed (Larrea et al. 2017). Fries (1953) estimated that in 1945, ~80% of the total pyroclastic material (tephra including the cone) had already been erupted, whereas only 25% of the total volume of lava was emitted during these first 2 years. By November 1946 (3 years and 10 months after the beginning of the eruption), more than 50% of the total lava volume had been erupted; the remaining 50% was extruded during the last 5 years of the eruption. Moreover, these changes in the eruption dynamics were accompanied by a progressive change in the bulk magma composition, evolving from an olivine-rich basaltic andesite with a SiO_2 content of ~53 wt.% to a pyroxene-rich andesite with ~60.5 wt.% SiO_2 (Wilcox 1954; McBirney et al. 1987; Larrea et al. 2019a, 2021). The final activity occurred on the February 25, 1952, when both lava flow emplacement and ash emission from the cone's crater ended abruptly. The post-eruption topography is now dominated by 'a'ā and rubbly block type lava flows with thicknesses from 5 to 30 m, mildly sloping surfaces (0° to 11°), and steep lobate margins (12° to 53°). The most prominent slopes in the area range from 28° to 53° and are associated with the Paricutin scoria cone (Figure S1 and Table S1 in Supplementary Material 1).

3 Methodology

3.1 Topographic reconstruction and working with Paricutin DEMs

The entire duration of the Paricutin eruption was systematically surveyed by geologists from several institutions including the US Geological Survey and the Universidad Nacional Autónoma de México, who monitored the growth of the cone, mapped the lava flows, and took samples, videos and photographs of the eruption (e.g., Trask 1945; Krauskopf and Williams 1946; Bullard 1947; Segerstrom 1950; Fries 1953). Luhr and Simkin (1993) presented a compilation of all of these previously available materials, which allowed Larrea et al. (2017) to create a geological map of the Paricutin eruptive sequence. The creation of this map for volumetric estimations required the reconstruction of the pre-eruptive topography for every single eruptive phase via the digitization and georeferencing of the maps representing the different eruptive phases defined by Luhr and Simkin (1993) (Fig. 1). The entire methodology for Paricutin's paleotopography reconstruction is presented in Larrea et al. (2017). A brief summary of the main methodological points is presented below. (a) Three topographic maps were used for the reconstruction: (1) INEGI (Instituto Nacional de Estadística, Geografía e Informática) E13B29, 1:50,000 topographic map (2015 edition; contour intervals: 20 m; WGS_1984 UTM) representing the post-eruption topography; (2) 1:10,000 USGS topographic map (USGS Bull. Vol. 965, 1956; contour intervals: 5 m) made from the aerial photographs taken by Compañía Mexicana Aerofoto S.A. in 1934, representing the pre-Paricutin topography in 1943; and (3) 1:10,000 USGS topographic map (USGS Bull. Vol. 965, 1956; contours interval: 5 m) made from the aerial photographs taken by Compañía Mexicana Aerofoto S.A. in 1946 for the US Geological Survey, representing the topography in 1946 during the eruption. (b) By using the pre-eruption topography and knowing the detailed areal footprint and thickness of each subsequent eruptive phase, the paleotopography of each lava flow was restored. (c) Once the topography "without lava flows" and "with lava flows" was obtained for each eruptive phase, 20-m-resolution DEMs were produced by Larrea et al. (2017) using an interpolation method of Triangular Irregular Network, in accordance with the available topographic information for the reconstructions.

The 20-m-resolution DEMs were prepared for their use as a simulation basis; first they were projected in a WGS84_UTM13N coordinate system, and then, the "Fill no-data" tool from raster analysis (QGIS 2.18) was applied to fill grid cell local holes in the DEMs, as described in Mossoux et al. (2016). The 23 phases defined by Luhr and Simkin (1993) based on direct eyewitness observations were slightly modified in terms of duration to include in one single eruptive phase the entire emplacement of each lava flow, from its initiation to its end (see also Larrea et al. 2017). Accordingly, the initial 23 eruptive phases are now regrouped in 22 lava eruptive phases to facilitate the simulation of each entire lava flow (Table 1; Fig. 1). **AQ3**

3.2 Simulating with Q-LavHA and determining model inputs

The existence of the sequential paleotopography maps for different eruptive phases enabled testing the user-friendly freeware lava flow simulation plug-in Q-LavHA (version 2.2.1) (Mossoux et al. 2016) for QGIS. This tool is a probabilistic code that can optionally include a deterministic calculation of the lava maximum runout, but this second option has not been

Table 1 Summary of lava flow parameters used for simulations with Q-LavHA 2.2.1 (Mossoux et al. 2016) for each eruptive phase of Paricutin volcano

Eruptive phase	Dates	Average thickness (m)	Area^a (m²)	Lava flow length (m)	Fissure (F) or vent (V)	F or V location	F distance between vents (m)	Simulation length (m)	H_c (m)	H_p (m)
1	February–August 1943	15^c	2,373,477	2000	F	X_f: 788,292; X_f: 788,797 Y_f: 2,157,302; Y_f: 2,157,864	100	20,000	15	–
2	September–December 1943	From 5 to 10^b	3,647,868	3600	Two V	X_{v1}: 788,343; X_{v2}: 789,066 Y_{v1}: 2,157,335; Y_{v2}: 2,158,166	–	V_1: 10,000 V_2: 36,000	10	–
3	January–August 1944	20^c	12,317,807	10,600	F	X_f: 789,002; X_f: 789,037 Y_f: 2,158,053; Y_f: 2,158,160	50	530,000	20	–
4	October 1944–January 1945	15^b	8,175,116	4500	F	X_f: 788,097; X_f: 788,271 Y_f: 2,157,354; Y_f: 2,157,275	50	45,000	15	–
5	February–May 1945	From 10 to 15^c	5,147,302	4400	Two V	X_{v1}: 788,044; X_{v2}: 788,331 Y_{v1}: 2,157,420; Y_{v2}: 2,157,264	–	V_1: 9000 V_2: 20,000	5	17
6	June–September 1945	10^c	2,316,008	4000	F	X_f: 788,028; X_f: 788,063 Y_f: 2,157,565; Y_f: 2,157,449	25	10,000	5	17
7	October 1945–February 1946	From 20 to 25^c	4,536,518	5200	V	X: 788,062 Y: 2,157,415	–	30,000	5	–
8	March–August 1946	10^b	5,089,923	5500	F and V	X_{iF}: 788,216; X_{fF}: 788,295; X_V: 789,167 Y_{iF}: 2,157,212; Y_{fF}: 2,157,245; Y_V: 2,157,807	F: 20	F: 20,000 V: 20,000	10	16
9	September–November 1946	From 10 to 25^c	2,365,852	2600	F	X_i: 788,091; X_f: 788,305 Y_i: 2,157,428; Y_f: 2,157,321	50	12,000	5	30
10	November–December 1946	20^b	2,698,805	2500	F	X_i: 787,853; X_f: 787,973 Y_i: 2,157,669; Y_f: 2,157,681	20	12,500	20	–
11	January–March 1947	20^c	2,650,329	2200	F	X_i: 788,362; X_f: 788,401 Y_i: 2,158,235; Y_f: 2,158,209	20	4500	5	18
12	April–August 1947	20^b	2,213,669	3100	V	X: 789,006 Y: 2,158,292	–	18,000	20	–

Natural Hazards

Table 1 (continued)

Eruptive phase	Dates	Average thickness (m)	Area[a] (m²)	Lava flow length (m)	Fissure (F) or vent (V)	F or V location		F distance between vents (m)	Simulation length (m)	H_c (m)	H_p (m)
13	August–December 1947	From 10 to 13[b]	2,581,915	2200	F and V	X_{iF}: 788,156 X_{fF}: 788,308 X_V: 788,947	Y_{iF}: 2,157,558 Y_{fF}: 2,157,387 Y_V: 2,158,114	F: 50	F: 7000 V: 3000	13	–
14	December 1947–June 1948	From 10 to 18[b]	4,155,393	4300	V	X: 788,817	Y: 2,158,253	–	32,000	18	35
15	May 1948–July 1949	From 9 to 25[c]	6,332,885	3400	F	X_i: 788,855 X_f: 788,960	Y_i: 2,157,998 Y_f: 2,157,854	50	8000	5	–
16	July 1949–August 1950	From 10 to 30[b]	4,292,047	3700	V	X: 788,817	Y: 2,157,931	–	12,000	9	–
17	April–October 1950	From 8 to 30[b]	1,601,109	3000	V	X: 788,896	Y: 2,158,088	–	11,000	10	–
18	October 1950–March 1951	From 7 to 20[b]	1,410,954	2600	V	X: 788,554	Y: 2,158,069	–	7000	12	–
19	February–March 1951	7[b]	369,042	1100	V	X: 788,810	Y: 2,158,082	–	2200	10	–
20	March 1951–January 1952	From 7 to 20[b]	5,474,067	4000	V	X: 789,094	Y: 2,158,279	–	60,000	20	–
21	January–February 1952	8[b]	812,085	1900	V	X: 788,895	Y: 2,157,709	–	6000	7	–
22	January–March 1952	8[b]	968,520	1900	V	X: 788,947	Y: 2,158,123	–	3800	7	–

For vent (X and Y) and fissure locations (initial "i" and final "f"), coordinates (UTM zone 13 N) are listed

H_c: Average thickness; H_p: corrective thickness parameter (details in Supplementary Material 3)

[a] Obtained from the supplemental topographic map published by the USGS (Bull, Vol, 965, 1956) and Luhr and Simkin (1993)

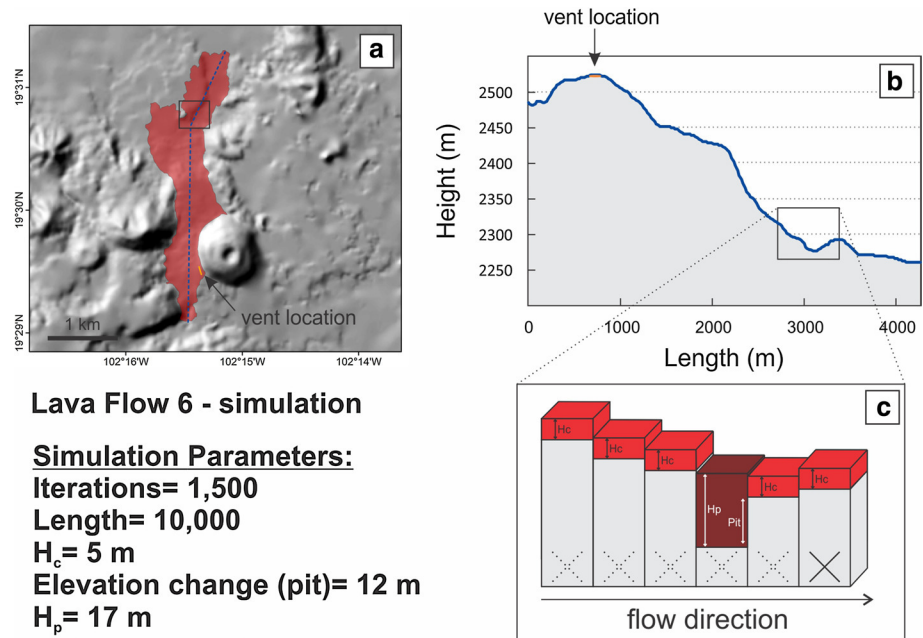[b] Thickness estimated by direct observation in the field as reported by Luhr and Simkin (1993)

[c] Thickness estimated by making profiles with the aid of the digital elevation model (see Larrea et al. 2017)

| Journal : **SmallCondensed 11069** | Article No : **4607** | Pages : **21** | MS Code : **4607** | Dispatch : **9-2-2021** |

Natural Hazards

170 considered for this work (VORIS—Felpeto et al. 2007; FLOWGO—Harris and Rowland
171 2001). It calculates the probability of lava flow spatial propagation from one or multiple regu-
172 larly distributed eruptive vents on a DEM. To overcome small topographic obstacles, the plug-
173 in includes corrective factors.

174 Using the aforementioned pre-eruption topography and knowing the accurate coverage of
175 each lava eruptive phase (Larrea et al. 2017, after Luhr and Simkin 1993), it was possible to
176 reproduce the area inundated of each lava flow by using combinations of the following input
177 parameters (Table 1): the preexisting topography, the vent or fissure location, the simulation
178 length (m), the number of iterations, the lava thickness (H_c, m) that is constant along the simu-
179 lation, a corrective thickness parameter (H_p, m), and 0.5–1% as fixed threshold (Supplemen-
180 tary Material 2). Other corrective parameters used for the simulations were the H_{16} option,
181 and the *Probability to the Square* option, (Mossoux et al. 2016). The vent or fissure-opening
182 location was established based on the historic reconstruction by Luhr and Simkin (1993) and
183 considering, when needed, the "aspect" to identify the more convenient downslope direction
184 for the simulation. In those cases, where the initial fissure or vent location was not giving
185 the desired simulation direction due to DEMs reconstruction artifacts, these vents or fissure
186 locations were slightly modified according to the most suitable aspect (downslope direction)
187 to obtain a good-fit flow propagation direction (see details in Supplementary Material 1);
188 in those simulations from a fissure, a distance between vents was also selected in order to
189 establish single effusive points along the fissure from which the lava would flow during the
190 simulation, as required by Q-LavHA (Mossoux et al. 2016; Table 1). Maximum lengths were
191 obtained from the real lava flows, which is from the vent to the front of each lobe. Since we
192 are working with a low-relief area and Q-LavHA considers the length reached by the lava flow
193 line at each iteration as a stopping parameter, the maximum simulated length of each lava
194 phase was increased with respect to the geodesic distance (see Discussion section for more
195 details). We used 1500 iterations for each of the 22 phases representing the number of runs
196 used to model each eruptive phase, (cf. Mossoux et al. 2016, and details in Supplementary
197 Material 2). Moreover, each 'a'ā-type lava flow was evaluated to identify sharp breaks in the
198 elevation profiles along the maximum length of the lava flow (see details in Supplementary
199 Material 3), such as topographical obstacles or pits (Fig. 2a, b). For the lava flows in which
200 those topographical obstacles or pits existed and were greater than the H_c (m), a corrective
201 factor (H_p) was then added and the H_{16} option activated (Table 1; Fig. 2c). A specific threshold
202 was used in order to keep only those grid cells having probabilities higher than a certain value
203 (see details in Supplementary Material 2).

204 Finally, by comparing the observed eruptive behavior of the volcano with the simulated
205 lava flow eruptive scenario for each respective phase, according to the areas covered by the
206 real vs simulated lava flows, we calculated the fitness indices (Table 2; Bertino et al. 2006;
207 Mossoux et al. 2016). These fitness indices evaluate the accuracy of the simulated lava flows,
208 based on the overlap area (well-simulated), the extra area covered by the simulation (overes-
209 timated area), and the real lava flow extension not covered by the simulation (underestimated
210 area). The underestimated areas are obtained by subtracting the percentage of well-simulated
211 areas from the 100% of each real lava flow area (Table 2).

| Journal : **SmallCondensed 11069** | Article No : **4607** | Pages : **21** | MS Code : **4607** | Dispatch : **9-2-2021** |

Natural Hazards

Fig. 2 Methodology used to evaluate the existence of pit holes or elevation changes along the lava flows profiles. **a** Example of Lava 6 where we define the profile route; **b** Lava flow 6 topographical profile showing elevation as a function of lava flow length along the profile route. Vent location and 12 m pit are also shown; **c** 3D schematic representation of the pit and the solution that Q-LavHA adopts to overcome it, activating H_p

4 Results and discussion

### 4.1 Lava simulations versus real lava flows at Paricutin

We simulated the 22 eruptive phases that occurred during the Paricutin eruption on previously reconstructed paleo-DEMs and obtained 22 different lava flow eruptive scenarios that approximate the real lava flows (Fig. 3a, b). The actual Paricutin lava flow areas range from 0.36 km^2 (lava No. 19) to 12.3 km^2 (lava No. 3, see Tables 1, 2). Minimum and maximum areas covered by the simulated lavas correspond to the smallest and largest eruptive scenario, respectively; the eruptive scenario 19 lava flow has an area of 0.41 km^2 (Fig. 3b; Table 2), and the scenario 3 lava flow has an area of 16.84 km^2 (Fig. 3a; Table 2).

When these areas are converted to percentages, the well-simulated areas range between 95 and 30% (Fig. 4; Table 2), with the first lava flow eruptive scenario (scenario 1 in Fig. 3a) being the most superimposed, and the 11th lava flow (scenario 11 in Fig. 3a) having the least overlap. The percentages obtained for the overestimated areas range between 16 and 71%, corresponding to the maximum and minimum values of the lava flow eruptive scenarios 6 and 12, respectively (Figs. 3a, 4b; Table 2). The percentages corresponding to underestimated areas range between 5 and 70%. Taking into account the well-simulated and overestimated areas, the simulated scenario that corresponds most closely to a real scenario is that of lava 17 (Fig. 3b; Table 2), for which the area was 83% well-simulated and

Table 2 Comparison of Paricutin eruptive phases with the best lava flow simulations obtained with Q-LavHA 2.2.1 (Mossoux et al. 2016) according to the parameters in Table 1

Eruptive phase	Dates	Real area (m²)	Simulation area (m²)	Well-simulated area (m²)	%	Overestimated area Area (m²)	%	Underestimated area (m²)
1	February–August 1943	2,373,477	5,566,400	2,260,623	95	3,305,777	59	112,854
2	September–December 1943	3,647,868	5,292,800	2,652,724	73	2,640,076	50	995,144
3	January–August 1944	12,317,807	16,847,600	9,591,679	78	7,255,921	43	2,726,128
4	October 1944–January 1945	8,175,116	16,318,800	7,452,735	91	8,866,065	54	722,381
5	February–May 1945	5,147,302	4,304,800	2,322,880	45	1,981,920	46	2,824,422
6	June–September 1945	2,316,008	1,794,400	1,498,788	65	295,612	16	817,220
7	October 1945–February 1946	4,536,518	5,617,700	3,436,346	76	2,181,354	39	1,100,172
8	March–August 1946	5,089,923	9,355,600	3,090,678	61	6,264,922	67	1,999,245
9	September–November 1946	2,365,852	3,760,000	1,111,823	47	2,648,177	70	1,254,029
10	November–December 1946	2,698,805	3,767,600	2,222,193	82	1,545,407	41	476,612
11	January–March 1947	2,650,329	1,018,400	803,637	30	214,763	21	1,846,692
12	April–August 1947	2,213,669	5,167,600	1,524,340	69	3,643,260	71	689,329
13	August–December 1947	2,581,915	3,918,400	1,805,945	70	2,112,455	54	775,970
14	December 1947–June 1948	4,155,393	8,304,800	3,037,850	73	5,266,950	63	1,117,543
15	May 1948–July 1949	6,332,885	4,822,400	3,576,520	56	1,245,880	26	2,756,365
16	July 1949–August 1950	4,292,047	4,051,200	1,740,611	41	2,310,589	57	2,551,436
17	April–October 1950	1,601,109	1,496,800	1,334,549	83	162,251	11	266,560
18	October 1950–March 1951	1,410,954	1,667,200	1,113,242	79	553,958	33	297,712
19	February–March 1951	369,042	409,200	257,670	70	151,530	37	111,372
20	March 1951–January1952	5,474,067	14,591,200	4,799,634	88	9,791,566	67	674,433
21	January–February 1952	812,085	1,208,800	569,892	70	638,908	53	242,193
22	January–March 1952	968,520	1,387,600	728,024	75	659,576	48	240,496
All Lava Flows	22 phases	24,792,658	27,314,100	23,269,086	94	4,045,013	16	1,523,571,87

The fitness indexes (well-simulated, overestimated, and underestimated areas) are calculated considering the area covered by the real and the simulated lava flows
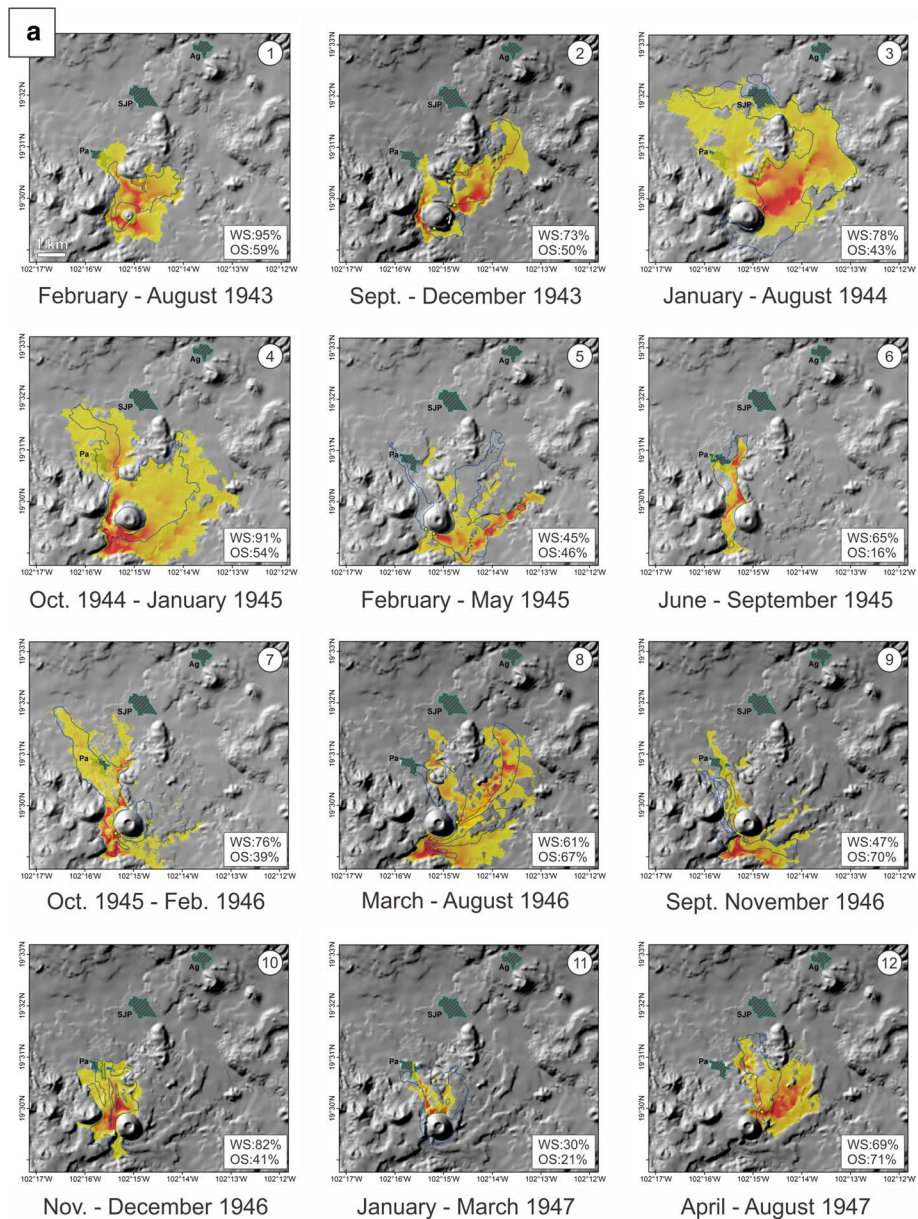
Fig. 3 Lava flow simulations by phases. **a** 12 first lava flow scenarios. **b** Scenarios 13–22 and a final map (*F*) combining the 22 lava flow simulations. Legend shows the probability of invasion in % and fitness indices values: WS: well-simulated and OS: oversimulated. Populated areas correspond to Pa: Paricutin, SJP: San Juan Parangaricutiro, and Ag: Angahuan

only 11% oversimulated. If the simulated areas are considered as a whole, the total area covered by the 22-lava flow eruptive scenarios spreads over 94% of the total area covered by the actual eruption, with 16% overestimation (Fig. 3b; Table 2).
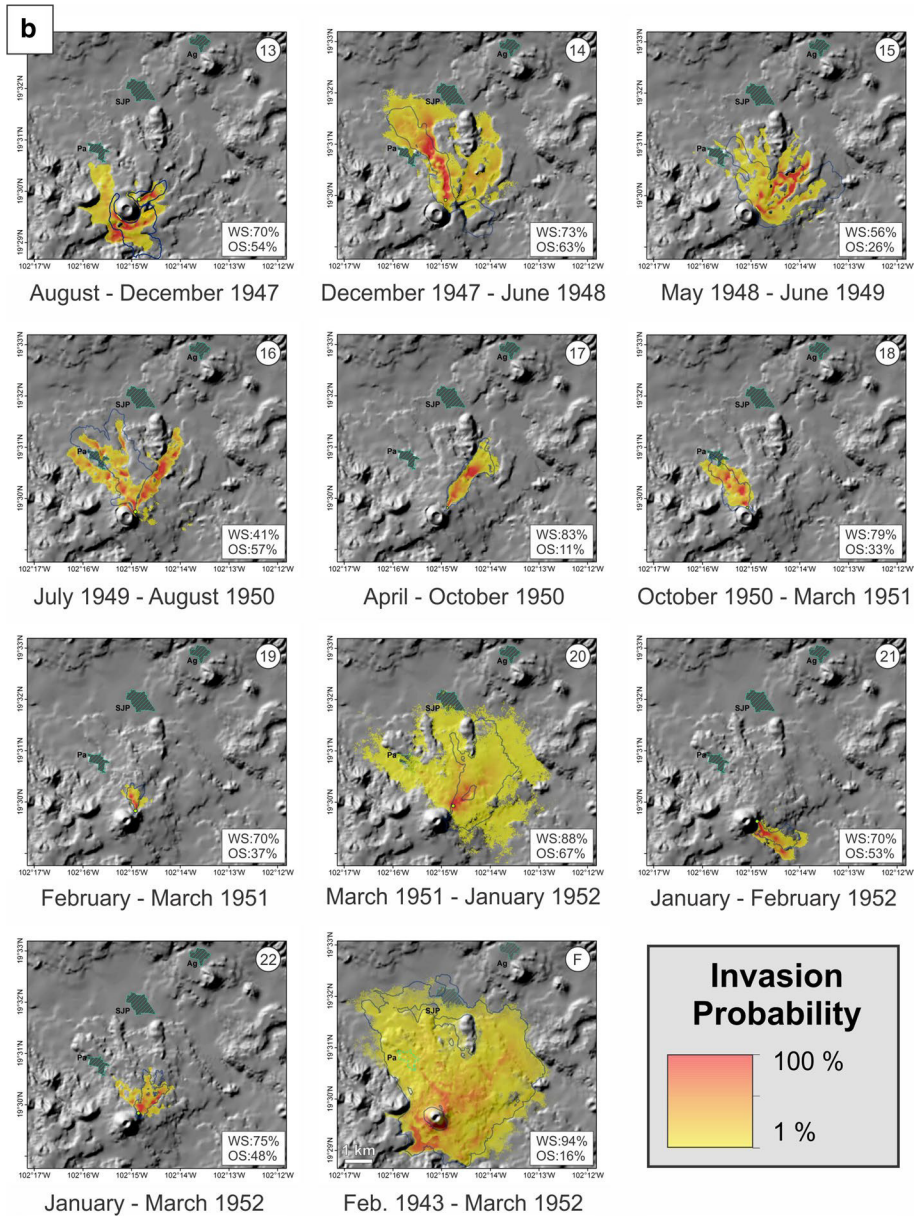
Fig. 3 (continued)

Comparing the areas of Paricutin's eruptive phases with the simulated eruptive scenarios for each respective phase, we observe that in most cases there is a degree of fit greater than 40% (Fig. 4). Scenarios 17, 18, and 19 represent the best simulations obtained, since the well-simulated areas are greater than 70% and the overestimated areas are less than 37% (Table 2; Fig. 4). However, there are some eruptive phases with poorer fit between the
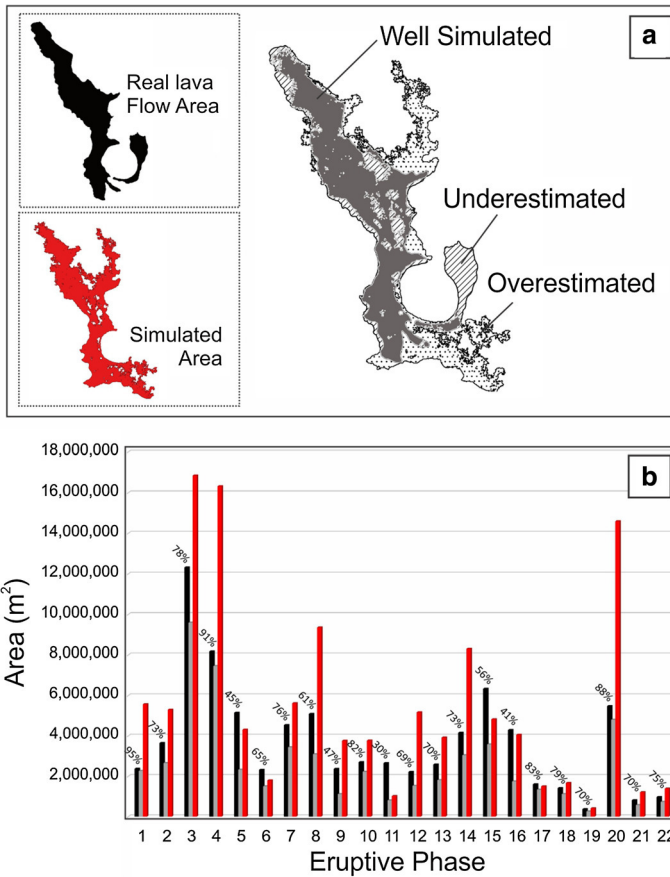
Fig. 4 **a** Schematic representation of the area covered by the real and the simulated lava (black) flow from eruptive phase 7, showing the well-simulated (gray), overestimated (dotted), and underestimated areas (striped). **b** Diagram showing the comparison of real Paricutin lava flow areas with the best lava flow simulations (data from Table 2). Note that the fitness percentages for each eruptive phase are calculated considering the area covered by the real and the simulated lava flows

239 simulation and the real lava flow extension; these simulation scenarios are 5, 9, 11, and 16,
240 where the well-simulated areas do not reach 50% and the overestimated areas vary from 21
241 to 70%. In order to obtain well-simulated areas greater than 70%, we needed to oversimu-
242 late by at least 50% of the real extension.

4.2 The tricky case of gentle slopes and low-relief terrains

244 The principal computational domain for predicting lava emplacement in most probabilistic
245 computer programs (be computational fluid dynamic models, volume or cooling limited
246 flows) and also in deterministic ones is topography, where lava flows tend to invade the
247 lowest-lying areas, or likewise, lava flows tend to follow the steepest paths (Mossoux et al.
248 2016, and references therein). In accordance, these probabilistic programs yield the best
249 results for moderate to high gradient topography. In contrast, on flat terrains, probabilistic

250 simulations of lava flows tend to follow a radial pattern or isotropic spreading (Dietter-
251 ich et al. 2017; Tarquini et al. 2019), hindering flow propagation and therefore impeding
252 accurate and reliable simulations. When lava flow simulations are done using probabilistic
253 models based on the maximum slope, volcanic areas with gentle sloping or flat topography
254 should be considered as special cases, and future probabilistic codes should better account
255 for this.

256 During the initial stages of this work, the preliminary simulations mainly focused on
257 the initial eruptive phases, using the real lava flow parameters. This did not yield good
258 results because the lavas were unable to spread in the actual direction of propagation or to
259 overcome the low initial slopes (e.g., 2.4° pre-eruption topography slope around the first
260 fissure; Supplementary Material 1). Simulated flows got stuck near the vent or fissure, with
261 a high probability of invasion around the vent/fissure that progressively decreased over a
262 short distance with a radial spread, resulting in a "fried egg effect". To solve this problem,
263 we had to enlarge the simulated lava length and activate the H_p parameter and the *Prob-*
264 *ability to the Square* option.

265 Another important characteristic of the first eruptive phases of the Paricutin eruption,
266 which probably played an important role in the emplacement and spread of the lava flows
267 on this low-relief terrain, was that initial pyroclastic deposits fell toward the southwest of
268 the initial vent following the main wind direction (Foshag and González-Reyna 1956), cre-
269 ating a new real-time relief that likely favored the propagation of the subsequent lava flows
270 toward the north-northeast (Fig. 3a).

4.3 Input parameter uncertainties in the Paricutin simulation and elsewhere

272 The paleotopography (i.e., DEM reconstruction) is used to allow the simulation to pro-
273 gress; however, the rest of the input parameters are the ones that confer realistic charac-
274 teristics to the simulated lava flows. Although carefully vetted input data are necessary for
275 meaningful results, it is also important to note that the input data will always have a certain
276 degree of uncertainty. Those uncertainties, as revealed in this work, are discussed below:

277 (a) *DEM resolution* the DEM resolution has a direct impact on the subsequent setting
278   of the initial parameter values on Q-LavHA (Mossoux et al. 2016). High-resolution
279   DEMs contain more geometric detail and allow more path possibilities (Mossoux et al.
280   2016), although they also increase the computational time in the simulations (Connor
281   et al. 2012). We have used a 20 m DEM resolution, which is adequate to carry out our
282   simulations, and we set up the Q-LavHA code accordingly.
283 (b) *Paleo-reconstruction—mapping errors* the most important and sensitive input param-
284   eter in Q-LavHA and any other code aimed at simulating gravity-driven flows (those
285   based on maximum slope and also deterministic codes) is the paleotopography or the
286   DEM. The 22 DEMs used here were reconstructed on the basis of the maps created
287   by Luhr and Simkin (1993), which are based on observations during the Paricutin
288   eruption. The paleo-reconstructions, as well as the digitization and georeferencing
289   processes, have minor intrinsic errors based on in situ observations that are difficult
290   to quantify (Larrea et al. 2017). The most complicated case corresponds to the ini-
291   tial topography before the first lava was emitted, as accurate control of the real-time
292   growth of the cone does not exist. The first lava started flowing on the February 21,
293   1943, the second day of the eruption. The first simulated lava flow (Fig. 3a, Scenario
294   1) presents an over-inundated area around the small paleo-reconstructed cone, where

(c) *Corrective factors* (H_c, H_p) Q-LavHA output does not represent the deposition of a specific lava volume or thickness on each inundated cell. Nevertheless, the program contemplates the real lava maximum or average thickness (H_c), which is considered as constant, and allows the use of a corrective parameter (H_p) that overcomes small topographical obstacles or pits when H_c cannot overcome them (Table 1). In this work, to simulate previous lava flows, it was necessary to analyze and identify present pits or obstacles on the topography (see details in Supplementary Material 3). We have identified topographical obstacles or pits in the elevation profiles of five eruptive phases that correspond to lavas 6, 8, 9, 11, and 14 (Supplementary Material 2). For these eruptive phases where real lava maximum thickness (H_c) could not overcome the obstacles, the corrective factor "H_p" has been estimated in order to favor the lava flow, ranging from 16 to 35 m for the five eruptive phases (Table S2, Supplementary Material 2, 3). Therefore, we note the importance of predetermining these depressions or small orographic hills on current topography in order to accurately simulate future lava flows.

(d) *Real versus simulated length* maximum lava lengths are commonly measured (from a map or DEM) from the initial vent or fissure to the front of the final lava lobe following a straight line in m. Nevertheless, in those models such as Q-LavHA where length is an input, each flow line follows a sinuous trajectory whose length is much longer than the straight distance measured along the main lava flow channel in the real flows. In addition, simulated lava flow lengths are influenced by the resolution of the DEM used and the slope of the volcanic area. Thus, maximum simulated lengths will normally have to be multiplied by a factor that will depend strongly on the abovementioned discrepancies. In the Paricutin simulations, maximum lava lengths were 2–50 times higher than the respective real lava flow lengths (Table 1). This range is slightly higher than the increase factor of ~ 1.5X that was applied in the gentle slope of Nyamuragira volcano (D.R. Congo) with a 30-m-resolution DEM (Mossoux et al. 2016).

(e) *Iterations* in order to evaluate the influence of the number of iterations in our simulations, we have simulated each eruptive phase with different iteration values: 1500, 2500, 5000, and 10,000. In all cases, as the number of iterations increases, a more widespread inundation is obtained, but the probability values associated with the extra grid cells are extremely low (e.g., two orders of magnitude smaller when using a higher number of iterations; see details in Supplementary Material 2). Therefore, comparing the simulations obtained with different numbers of iterations and considering the suggested 1% threshold (Mossoux et al. 2016), it is shown that too few iterations produce results that are not representative of the real lava inundation area; in contrast, a high number of results that converge on a value establish more confidence in the results while increasing the computation time. Based on these results, we have established that 1500 iterations constitute a good balance between time and inundation area.

(f) *Thresholds* from 0.5 to 1% were used for the complete simulations in order to keep only those grid cells having probabilities higher than a certain value (Supplementary Material 2). In our particular case, probabilities below that threshold are considered noise and are neglected. Thresholds are easier to establish when working with eruptions that have taken already place since we can compare the past with the simulated scenario. Importantly, we note that whether or not low threshold probabilities are considered can have a significant impact on the resulting simulation. In the case of the Paricutin eruptive phase 3, a threshold of 0% is required to produce a broad inundation

344   area that includes the small village of San Juan Parangaricutiro, which was actually
345   flooded and evacuated on the 19th of June, 1944 (Luhr and Simkin 1993, Fig. 3a),
346   whereas neglecting the lowest probabilities leads to a simulation that does not entirely
347   flood this village. Also, when working with real-time or future scenarios, to keep low
348   probabilities on the map could be useful in order to remark safer areas. This fact is
349   important to consider when developing mitigation measures and evacuation plans in
350   future eruptions elsewhere. In accordance, the threshold has to be carefully chosen for
351   hazard map constructions.

4.4 Future volcanic hazard assessment

353 The Paricutin eruption represents the most recent eruption in the MGVF, which is the
354 largest subduction-related monogenetic distributed field in the world including over 1100
355 scoria cones and associated lava flows, ~ 400 medium-sized volcanoes (Mexican shields,
356 e.g., Chevrel et al. 2016), ~ 22 phreatomagmatic vents (maars and tuff cones, e.g., Kshirsa-
357 gar et al. 2015), as well as isolated domes and lava flows (e.g., Mahgoub et al. 2018).
358 A seismic swarm related to dike emplacement, with more than 700 earthquakes with
359 moment magnitudes exceeding 2.4 on the Richter scale (Gardine et al. 2011; Pizón et al.
360 2017), occurred in June 2006, 15 km WSW of the summit of the Paricutin cone. More
361 recently (January–February 2020), another seismic swarm (> 5000 recorded earthquakes)
362 has taken place in the Paricutin area with moment magnitudes up to 4.1, and hypocent-
363 ers at ~ 10–20 km depth (Servicio Sismológico Nacional 2020). The historic eruptions of
364 Paricutin (1943) and Jorullo in 1759 (Guilbaud et al. 2011), together with these seismic
365 swarms, indicate that this area is still volcanically active, and therefore, more eruptions
366 within the MGVF should be expected in the future, posing risks (e.g., distal ash fallout) to
367 large population centers including Mexico City (Siebe and Macias 2006).
368   Moreover, small monogenetic vents (scoria cones and isolated vents) are not distributed
369 evenly throughout the MGVF, occurring either as isolated centers or forming small clus-
370 ters. The identification of three Holocene temporal and spatial clusters, namely Tacámbaro
371 (Guilbaud et al. 2012; Mahgoub et al. 2017), Malpaís de Zacapu (Reyes-Guzmán et al.
372 2018; Mahgoub et al. 2018), and Tancítaro (Larrea et al. 2019b), poses key questions in
373 regard to future volcanic hazard assessments in the MGVF. These clusters comprise several
374 volcanoes in areas of a few tens of km^2 that erupted within hundreds to a few thousands
375 of years of one another leading to questions of "where" and "when" the next monogenetic
376 eruptions in the MGVF are likely to occur, and whether they will be single short-lived
377 isolated eruptions, the beginning of a new cluster, or the continuation of previously exist-
378 ing ones (Larrea et al. 2019b). In this regard, it is possible that the historic eruptions of
379 Jorullo and Paricutin could each represent the beginning of a cluster and that a new erup-
380 tion in their proximity could be expected in the future. However, studies dealing with erup-
381 tion recurrence rates, spatial and temporal distribution of eruptive centers, composition and
382 eruptive style, and the tectonic control of volcanism in the MGVF are still too scarce to
383 facilitate comprehensive hazard assessments and development of monitoring strategies. In
384 accordance, the next step in volcanic hazards assessment in the MGVF would be the con-
385 struction of a volcanic susceptibility map. Such maps show the spatial probability of future
386 eruptions and are constructed by combining the available geological and structural data
387 through a kernel density estimation and a nonhomogeneous Poisson process (e.g., Cappello
388 et al. 2013; Connor et al. 2019; and references therein). The MGVF volcanic susceptibility
389 map will represent the basis for further eruptive scenario analyses.

5 Conclusions

For the development of volcanic hazard maps, it is common to set all of the input parameters based on the characteristics of lavas from the geological or historical record, which, in probabilistic simulations, are normally considered to be constant throughout the whole eruption (e.g., Bartolini et al. 2014; Becerril et al. 2017). In the work presented here, we demonstrate that each phase of an eruption is governed by unique parameters that must be considered when using probabilistic models such as Q-LavHA, when tracking a similar scenario. This fact reflects the need to improve lava flow models to handle the variable phases of long-lived eruptions since these are not rare events. Moreover, we stress the importance of the role of the paleotopography and the parameters used in each simulation when using lava flow models. General suggestions to take into account from this work forward include the following:

- Topography: accurate and medium high-resolution topography (e.g., 10–30 m) will play the most important role in the predicted lava flow spreading. Low-relief topography has to be considered specially, and the other input parameters must be set carefully according to the characteristics of the gently sloped area under study. We also note the importance of predetermining depressions or small orographic hills on the preexisting topography in order to accurately simulate future lava flows.
- Length: in probabilistic programs where lava length is a fundamental parameter, it will normally be necessary to increase the simulated lengths used in order to reach the total real lava extent. The required increase will depend on how flat or steep topography is, and also on the DEM resolution.
- Thickness: it is important to consider thickness variations during simulations since it may help to improve the obtained results (e.g., ELMF in Damiani et al. 2006).
- Iterations: in the probabilistic program Q-LavHA, and for the specific case of Paricutin volcano, a minimum number of iterations (1,500) will be sufficient to obtain good simulation results. Nevertheless, a sensitivity analysis with this parameter should be done for each study area to obtain the minimum number of iterations needed to produce sufficiently high-quality results.
- Threshold: it is important to verify whether or not it is necessary to consider probabilities below a certain threshold; this parameter has to be carefully chosen for hazard map constructions, to avoid either over- and underpredicting the lava flooding zone, the latter potentially resulting in the neglect of invasion zones that could affect villages or infrastructures.
- Fitness indices: to better evaluate the accuracy of the simulated lava flows, it is also important to calculate the overlapped area, the extra area, and the real lava flow extension not covered by the simulation. The well-simulated, overestimated, and underestimated values will depend on the simulations done for a particular location/volcano.
- Q-LavHA future updating: Q-LavHA is characterized by a user-friendly interface and flexibility allowing the user to perform long-term volcanic hazard assessment and short-term hazard forecasting. Nevertheless, some improvements could be incorporated to perform better simulations in gently sloping terrains. A recent work by Tarquini et al. (2019) applies a new probabilistic code "MrLavaLoba" (de'Michieli Vitturi and Tarquini 2018), which incorporates an inertial factor that aims to facilitate the flow propagation approximately along the previously established direction.

| Journal : **SmallCondensed 11069** | Article No : **4607** | Pages : **21** | MS Code : **4607** | Dispatch : **9-2-2021** |

Natural Hazards

In this regard, similar gradient factors could be incorporated in Q-LavHA in the near future to better overcome the absence of an elevation gradient.

We would like to point out that, based on the aforementioned, future simulations of lava flows should consider the possibility of nonconstant parameters and should employ a comprehensive analysis of each lava phase during an eruption to better control the parameters that impact the simulations. This will be crucial for formulating mitigation measures and evacuation plans in similar scenarios of future eruptions, as informed decisions based on accurate simulations could help avoid severe social and economic consequences. **AQ4**

Authors' contributions L.B. and P.L. conceived and developed the original idea and took the lead in writing the manuscript, designed the figures, tables, and supplementary material. L.B. performed the numerical simulations with the input of P.L., S.M, D.F, and S.S. The reconstructed paleotopography and DEMs were fully created by S.S. All authors provided critical feedback and helped shape the research and approved the final manuscript.

Code availability Not applicable.

Compliance with ethical standards

Conflict of interest The authors declare that they have no conflict of interest.

References

Bartolini S (2014) Volcanic hazard assessment in monogenetic volcanic fields. PhD dissertation. University of Barcelona

Bartolini S, Geyer A, Martí J, Pedrazzi D, Aguirre-Díaz G (2014) Volcanic hazard on Deception Island (South Shetland Islands). J Volcanol Geotherm Res. https://doi.org/10.1016/j.jvolgeores.2014.08.009

Bertin D, Lindsay JM, Becerril L, Cronin SJ, Bertin LJ (2019) MatHaz: a Matlab code to assist with probabilistic spatio-temporal volcanic hazard assessment in distributed volcanic fields. J Appl Volcanol 8(1):4

Becerril L, Martí J, Bartolini S, Geyer A (2017) Assessing qualitative long-term volcanic hazards at Lanzarote Island (Canary Islands). Nat Hazards Earth Syst Sci 2017(17):1145–57

Bertino E, Damiani ML, Groppelli G, Norini G, Aldighieri B, Borgonovo S, Comoglio F, Pasquaré G (2006) Modelling lava flow to assess hazard on Mount Etna (Italy). From geological data to a preliminary hazard Map. International Congress on Environmental Modelling and Software, p 345

Booth B (1979) Assessing volcanic risk. J Geol Soc London 136:331–340

Bullard FM (1947) Studies on Paricutin volcano. Geol Soc Am Bull 58:433–449

Cappello A, Bilotta G, Neri M, Negro CD (2013) Probabilistic modeling of future volcanic eruptions at Mount Etna. J Geophys Res Solid Earth 118(5):1925–1935

Chevrel MO, Siebe C, Guilbaud M-N, Salinas S (2016) The AD 1250 El Metate shield volcano (Michoacán): Mexico's most voluminous Holocene eruption and its significance for archeology and hazards. The Holocene 26(3):471–488

Cordonnier B, Lev E, Garel F (2016) Benchmarking lava-flow models. Geol Soc London Spec Publ 426:425–445. https://doi.org/10.1144/SP426.7

Connor CB (1987) Structure of the Michoacán–Guanajuato volcanic field. Mexico J Volcanol Geotherm Res 33(1–3):191–200

Connor LJ, Connor CB, Meliksetian K, Savov I (2012) Probabilistic approach to modeling lava flow inundation: a lava flow hazard assessment for a nuclear facility in Armenia. J Appl Volcanol 1:1–19. https://doi.org/10.1186/2191-5040-1-3

Connor CB, Connor LJ, Germa A, Richardson JA, Bebbington M, Gallant E, Saballos JA (2019) How to use kernel density estimation as a diagnostic and forecasting tool for distributed volcanic vents. Stat Volcanol 4(3):1–25

Crisci GM, Avolio MV, Behncke B, D'Ambrosio D, Di Gregorio S, Lupiano V, Neri M, Rongo R, Spataro W (2010) Predicting the impact of lava flows at Mount Etna. Italy J Geophys Res 115:B04203. https://doi.org/10.1029/2009JB006431

Damiani ML, Groppelli G, Norini G, Bertino E, Gigliuto A, Nucita A (2006) A lava flow simulation model for the development of volcanic hazard maps for Mount Etna (Italy). Comput Geosci 32(4):512–526

de' Michieli Vitturi M, Tarquini S (2018) MrLavaLoba: a new probabilistic model for the simulation of lava flows as a settling process. J Volcanol Geotherm Res 349:323–334

Dietterich HR, Lev E, Chen J, Richardson JA, Cashman KV (2017) Benchmarking computational fluid dynamics models of lava flow simulation for hazard assessment, forecasting, and risk management. J Appl Volcanol 6(1):9

Felpeto A, Martí J, Ortiz R (2007) Automatic GIS-based system for volcanic hazard assessment. J Volcanol Geotherm Res 166:106–116

Foshag WF, González-Reyna J (1956) Birth and development of Parícutin volcano, Mexico. US Geol Surv Bull 965D:355–485

Fries C (1953) Volumes and weights of pyroclastic material, lava and water erupted by Parícutin volcano, Michoacán. Mexico Trans Am Geophys Union 34(4):603–616

Gardine M, West ME, Cox T (2011) Dike emplacement near Parícutin volcano, Mexico in 2006. Bull Volcanol 3:123–132

Granados HD, Jenkins S (2015) Extreme volcanic risks 1: Mexico City. Volcanic hazards, risks and disasters. Elsevier, Amsterdam, pp 315–354

Guilbaud MN, Siebe C, Layer P, Salinas S, Castro-Govea R, Garduno-Monroy VH, Le Corvec N (2011) Geology, geochronology, and tectonic setting of the Jorullo Volcano region, Michoacan, Mexico. J Volcanol Geotherm Res 201:97–112

Guilbaud M-N, Siebe C, Layer P, Salinas S (2012) Reconstruction of the volcanic history of the Tacámbaro-Puruarán area (Michoacán, México) reveals high frequency of Holocene monogenetic eruptions. Bull Volcanol 74(5):1187–1211

Harris AJL, Rowland SK (2001) FLOWGO: a kinematic thermo-rheological model for lava flowing in a channel. Bull Volcanol 63:20–44. https://doi.org/10.1007/s004450000120

Hasenaka T (1994) Size, distribution, and magma output rate for shield volcanoes of the Michoacán–Guanajuato volcanic field, Central Mexico. J Volcanol Geotherm Res 63:13–31

Hasenaka T, Carmichael ISE (1985) The cinder cones of Michoacán–Guanajuato, Central Mexico: their age, volume and distribution, and magma discharge rate. J Volcanol Geotherm Res 25:105–124

Inbar M, Lugo Hubp J, Villers Ruiz L (1994) The geomorphological evolution of the Paricutin cone and lava flows, Mexico, 1943–1990. Geomorphol 9:57–76

Kereszturi G, Németh K (2012) Monogenetic basaltic volcanoes: genetic classification, growth, geomorphology and degradation. Updates in volcanology-new advances in understanding volcanic systems. IntechOpen, Hamilton

Krauskopf K, Williams H (1946) The activity of Parícutin during its third year. Trans Am Geophys Union 27:406–410

Journal : **SmallCondensed 11069** | Article No : **4607** | Pages : **21** | MS Code : **4607** | Dispatch : **9-2-2021**

Natural Hazards

Kshirsagar P, Siebe C, Guilbaud M-N, Salinas S, Layer PW (2015) Late Pleistocene Alberca de Guadalupe maar volcano (Zacapu basin, Michoacán): stratigraphy, tectonic setting, and paleohydrogeological environment. J Volcanol Geoth Res 304:214–236

Larrea P, Salinas S, Widom E, Siebe C, Abbitt RJF (2017) Compositional and volumetric development of a monogenetic lava flow field: the historical case of Paricutin (Michoacán, Mexico). J Volcanol Geotherm Res 348:36–48

Larrea P, Widom E, Siebe C, Salinas S, Kuentz D (2019a) A re-interpretation of the petrogenesis of Paricutin volcano: Distinguishing crustal contamination from mantle heterogeneity. Chem Geol 504:66–82

Larrea P, Siebe C, Juárez-Arriaga E, Salinas S, Ibarra H, Böhnel H (2019b) The~ AD 500–700 (Late Classic) El Astillero and El Pedregal volcanoes (Michoacán, Mexico): a new monogenetic cluster in the making? Bull of Volcanol 81(10):59

Larrea P, Albert H, Ubide T, Costa F, Colás V, Widom E, Siebe C (2021) From explosive vent opening to effusive outpouring: mineral constraints on magma dynamics and timescales at Paricutin monogenetic volcano. J Petrol. https://doi.org/10.1093/petrology/egaa112

Loughlin SC, Sparks RSJ, Sparks S, Brown SK, Jenkins SF, Vye-Brown C (eds) (2015) Global volcanic hazards and risk. Cambridge University Press, Cambridge

Luhr JF, Simkin T (1993) Parícutin. The Volcano born in a Mexican cornfield. Geoscience Press, Phoenix

Mahgoub AN, Böhnel H, Siebe C, Salinas S, Guilbaud M-N (2017) Paleomagnetically inferred ages of a cluster of Holocene monogenetic eruptions in the Tacámbaro-Puruarán area (Michoacán, México): implications for volcanic hazards. J Volcanol Geoth Res 347:360–370

Mahgoub AN, Reyes-Guzmán N, Böhnel H, Siebe C, Pereira G, Dorison A (2018) Paleomagnetic constraints on the ages of the Holocene Malpaís de Zacapu lava flow eruptions, Michoacán (Mexico): implications for archeology and volcanic hazards. Holocene 28(2):229–245

McBirney AR, Taylor HP, Armstrong RL (1987) Paricutin re-examined: a classic example of crustal assimilation in calc-alkaline magma. Contrib Mineral Petrol 95:4–20

Mossoux S, Saey M, Bartolini S, Poppe S, Canters F, Kervyn M (2016) Q-LAVHA: A flexible GIS plugin to simulate lava flows. Comput Geosci 97:98–109

Nolan ML, Gutiérrez C (1979) Impact of Parícutin on five communities. In: Activity Volcanic, Ecology Human (eds) Sheets and Grayson. Academic Press, New York, pp 293–338

Ordoñez E (1943) The new volcano of Paricutin. University of Texas, Institute of Latin American Studies, Texas, pp 62–78

Pizón JI, Núñez-Cornú FJ, Rowe CA (2017) Magma intrusion near Volcan Tancitaro: evidence from seismic analysis. Phys Earth Planet Inter 262:66–79

Reyes-Guzmán N, Siebe C, Chevrel MO, Guilbaud MN, Salinas S, Layer P (2018) Geology and radiometric dating of Quaternary monogenetic volcanism in the western Zacapu lacustrine basin (Michoacán, México): implications for archaeology and future hazard evaluations. Bull Volcanol 80:18

Rymer H (2015) Part VII volcanic hazards. In: Sigurdsson H (ed) The encyclopedia of volcanoes, 2nd edn. Elsevier, Amsterdam, pp 895–896

Segerstrom K (1950) Erosion studies at Parícutin, State of Michoacán, Mexico. U.S. Geol Surv Bull 965A:1–164

Siebe C, Macias JL (2006) Volcanic hazards in the Mexico City metropolitan area from eruptions at Popocatepetl, Nevado de Toluca, and Jocotitlan stratovolcanoes and monogenetic scoria cones in the Sierra Chichinautzin volcanic field. In: Siebe C, Macias JL, Aguirre-Diaz GJ (eds) Neogene-quarternary continental margin volcanism: a perspective from México, vol 402. Geological Society of America, Boulder, pp 253–329

SSN (2020) Servicio Sismológico Nacional, Instituto de Geofísica, Universidad Nacional Autónoma de México, México. http://www.ssn.unam.mx

Tarquini S, Favalli M, Mazzarini F, Isola I, Fornaciai A (2012) Morphometric analysis of lava flow units: case AQ5 study over LIDAR-derived topography at Mount Etna, Italy. J Volcanol Geoth Res 235:11–22

Tarquini S, Vitturi MDM, Jensen E, Pedersen G, Barsotti S, Coppola D, Pfeffer MA (2019) Modeling lava flow propagation over a flat landscape by using MrLavaLoba: the case of the 2014–2015 eruption at Holuhraun. Iceland Annals of Geophysics 62(2):228

Trask P (1945) The Mexican volcano Paricutin. Science 95:501–505

Valentine GA, Connor CB (2015) Basaltic volcanic fields. In: Sigurdsson H, Houghton BF, McNutt SR, Rymer H, Stix J (eds) Encyclopedia of Volcanoes, 2nd edn. Academic Press, London, pp 423–439

594 Walker GPL (2000) Basaltic volcanoes and volcanic systems. In: Sigurdsson H, Houghton BF, McNutt SR,
595   Rymer H, Stix J (eds) Encyclopedia of volcanoes. Academic Press, San Diego, pp 283–290
596 Wilcox RE (1954) Petrology of Parícutin Volcano, Mexico. U.S. Geol Surv Bull 965C:281–353
597 Yokoyama I, De la Cruz-Reyna S (1990) Precursory earthquakes of the 1943 eruption of Paricutin volcano,
598   Michoacan. Mexico J Volcanol Geotherm Res 44(3–4):265–281

Authors and Affiliations

Laura Becerril[1,2] [ORCID] **· Patricia Larrea[3,4] · Sergio Salinas[5] · Sophie Mossoux[6] ·
Dolors Ferrés[7] · Elisabeth Widom[4] · Claus Siebe[8] · Joan Martí[2]**

1   Geological Survey of Chile (SERNAGEOMIN), Teatinos 50, Santiago de Chile, Chile

2   Institute of Earth Sciences Jaume Almera, Spanish Scientific Research Council, 08028 Barcelona,
     Spain

3   Department of Geology and andean Geothermal Center of Excellence (CEGA), Facultad de
     Ciencias Físicas y Matemáticas, Universidad de Chile, Plaza Ercilla 803, Santiago, Chile

4   Department of Geology and Environmental Earth Science, Miami University, Oxford, OH 45056,
     USA

5   Facultad de Ingeniería, División de Ingeniería en Ciencias de la Tierra, Universidad Nacional
     Autónoma de México, Ciudad Universitaria, C.P. 04510 Coyoacán, Mexico City, Mexico

6   Department of Geography, Vrije Universiteit Brussel, 1050 Brussel, Belgium

7   Escuela Nacional de Ciencias de la Tierra, Universidad Nacional Autónoma de México, Ciudad
     Universitaria, C.P. 04510 Coyoacán, Mexico City, Mexico

8   Departamento de Vulcanología, Instituto de Geofísica, Universidad Nacional Autónoma de
     México, Ciudad Universitaria, C.P. 04510 Coyoacán, Mexico City, Mexico